

FIRST DIRECT METALLICITY MEASUREMENT OF A LENSED STAR-FORMING GALAXY AT $z = 1.7^*$

T.-T. YUAN AND L. J. KEWLEY

Institute for Astronomy, University of Hawaii, 2680 Woodlawn Drive, Honolulu, HI 96822, USA

Received 2009 March 31; accepted 2009 May 29; published 2009 June 25

ABSTRACT

We present the rest-frame optical spectrum of a strongly lensed galaxy at redshift $z = 1.7$ behind the cluster Abell 1689. We detect the temperature sensitive auroral line [O III] $\lambda 4363$, which allows the first *direct* metallicity measurement for galaxies at $z > 1$. Our high signal-to-noise spectrum indicates that the target is an extremely low metallicity star-forming galaxy, with $12 + \log(\text{O}/\text{H}) = 7.5^{+0.1}_{-0.2}$ from the direct T_e -based method. We estimate an intrinsic absolute B -band magnitude of $M_B = -18.3 \pm 0.1$, with a stellar mass of $4.4 \pm 1.2 \times 10^8 M_\odot$. This galaxy extends the luminosity–metallicity relation of star-forming galaxies at $z > 2$ by more than an order of magnitude. Given the double nuclei-like morphology and the velocity profile of H α , we tentatively suggest that it could be a merger or a proto-rotating disk galaxy.

Key words: galaxies: abundances – galaxies: evolution – galaxies: high-redshift

1. INTRODUCTION

Five years ago, our knowledge about galaxy evolution still had a glaring gap between redshifts 1.5 and 3, termed the redshift desert. The desert is even more desolate for galaxy chemical evolution studies, where high signal-to-noise (S/N) spectra are needed for reliable measurements. However, great progress has been made in the last few years in studying galaxies at $z \sim 2$ and we are beginning to harvest the “desert.” To date, metallicities are available for a few tens of individual galaxies at $1.5 < z < 3$ (Shapley et al. 2004; Erb et al. 2003, 2006; Hayashi et al. 2009). These galaxies are selected using broadband colors either in the UV (Lyman Break technique; Steidel et al. 1996, 2003) or using B -, z -, and K -band colors (BzK selection; Daddi et al. 2004). The Lyman break and BzK selection techniques favor the galaxies that are luminous in the UV or blue and could therefore be biased against low-luminosity (low-metallicity) galaxies, and dusty (potentially metal-rich) galaxies.

To date, metallicity measurements for high-redshift ($z \geq 1$) galaxies have been made via indirect methods from the ratios of strong nebular lines. In local galaxies, the preferred method for determining metallicity is via the “direct” T_e method which relies on the electron temperature sensitivity of the [O III] $\lambda 4363$ line. At high redshift, metallicity measurement via the direct method has not been possible because the [O III] $\lambda 4363$ line used to derive the electron temperature is very weak. The highest redshift that the [O III] $\lambda 4363$ line has been reported is at $z \sim 0.8$ by Hoyos et al. (2005) and Kakazu et al. (2007).

Strong lensing by galaxy clusters offers an alternative tool to explore the metallicity of galaxies at high redshift. One advantage of lensing selected galaxies is that they are immune to color and luminosity biases. Previously, only five lensed galaxies had been observed with sufficient spectral coverage and S/N to yield metallicities (Yee et al. 1996; Pettini et al. 2000, 2002; Lemoine-Busserolle et al. 2003; Nesvadba et al. 2007; Stark et al. 2008). Compared with Lyman break selected galaxies in the same redshift and luminosity range, the five lensed objects span a substantially broader metallicity range ($12 + \log(\text{O}/\text{H}) \sim 7.1\text{--}9.1$), indicating that current metallicity history studies at $z > 1.5$ ($12 + \log(\text{O}/\text{H}) \sim 8.4\text{--}8.8$) may not be sampling

the full metallicity range at this redshift. It is worth noting that the metallicity range quoted for the lensed galaxies is extremely uncertain, depending on various assumptions about reddening and metallicity calibrators. Another great advantage of gravitational lensing is its natural magnification of the source. The flux of the lensed background galaxy is commonly boosted by a factor of 1–3 mag or more around the critical lines of the cluster center. Optical spectroscopic surveys of high- z galaxies near cluster critical lines have already yielded a large catalog of lensed galaxies beyond $z \sim 1$ (e.g., Broadhurst et al. 2005; Richard et al. 2008; Frye et al. 2007; Limousin et al. 2007). Unfortunately, spectra from these surveys cannot be directly utilized in metallicity studies because the commonly used metallicity diagnostic emission lines have shifted into the near-infrared (near-IR) at $z > 1$.

With the revolutionary multiobject cryogenic near-IR spectrographs that have been recently installed on 8–10 m class telescopes, high efficiency near-IR spectroscopy is now available. We carried out the first near-IR spectroscopic survey of lensed galaxies behind lensing clusters, aimed at measuring the metallicity of galaxies at $1.5 < z < 3$. This Letter reports the rest-frame optical spectrum of a strongly lensed star-forming galaxy at $z = 1.7$ behind the Abell cluster 1689 from our on-going survey. The galaxy cluster Abell 1689 was chosen as our first target because it has the largest Einstein radius of $\sim 50''$ (Broadhurst et al. 2005), and nearly ~ 100 spectroscopically confirmed lensed images (Limousin et al. 2007). The galaxy in question is designated as ID 22.3 in the catalog of Broadhurst et al. (2005), we refer to it as Lens22.3 hereafter. Throughout we use the standard Λ cold dark matter (Λ CDM) cosmology with $H_0 = 70 \text{ km s}^{-1} \text{ Mpc}^{-1}$, $\Omega_M = 0.3$, and $\Omega_\Lambda = 0.7$.

2. OBSERVATIONS AND DATA REDUCTION

The data were obtained on 2008 March 26, using the Multi-Object InfraRed Camera and Spectrograph (MOIRCS) at Subaru (Ichikawa et al. 2006), in the spectroscopic mode (Tokoku et al. 2006). We used the low-resolution grism zJ 500 with a nominal resolution of 500 and a wavelength coverage of 0.9–1.78 μm . We designed two masks targeting the spectroscopically confirmed lensed images in the field of Abell 1689. We obtained useable data for one mask. During the observation for this mask, the seeing varied between $0''.3$ and $0''.6$, and the

* Based on data collected at Subaru Telescope, which is operated by the National Astronomical Observatory of Japan.

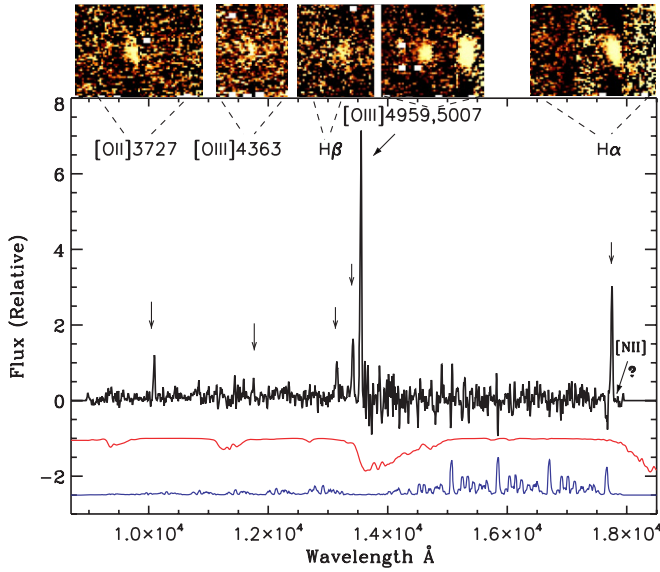


Figure 1. Observed *Subaru* MOIRCS spectrum of Lens22.3 at $z = 1.7$. The extracted one-dimensional spectrum is shown in black, with the identified emission lines labeled. The sky telluric absorption and OH emission lines are shown in red and blue, respectively. The two-dimensional spectrum for each of the detected lines is shown on top.

air mass ranged between 1.1 and 1.7. Lens22.3 was placed at one of the center slits of the mask, with a slit width of $\sim 1''$ and a slit length of $\sim 9''$. The telescope was nodded along the slit in a ABAB mode with a dithering length of $2''.5$. The exposure time for each individual frame was 400–600 s, resulting in a total integration time of 6800 s.

We reduced the data using the standard IRAF and IDL routines. Sky OH lines were removed by subtracting the closest dithering pair A and B. A scaling factor between each pair was determined to optimize the sky subtraction. The sky-subtracted A–B pair was flat-fielded, cleaned for cosmic rays, and then traced and rectified using a dome flat spectrum. The final two-dimensional spectrum was created by co-adding the reduced individual pairs. Wavelength calibration was carried out using the strong OH lines between 0.9 and $1.8 \mu\text{m}$. An F5V standard star was observed at approximately the same air mass as the target. The Telluric absorption was obtained by dividing the star spectrum with a fitted blackbody curve. The resulting stellar spectrum was then divided into the object spectrum to correct for telluric absorption.

3. ANALYSIS AND RESULTS

3.1. Metallicity

At redshift 1.7, all the rest-frame optical metallicity diagnostic lines fall into the spectral coverage of MOIRCS zJ500 grism. We have detected all the rest-frame nebular emission lines from [O II] to $\text{H}\alpha$, including the usually very weak [O III] $\lambda 4363$ line. Figure 1 shows our final two-dimensional and one-dimensional rest-frame optical spectrum of Lens22.3. Table 1 lists the measured line fluxes relative to $\text{H}\beta$, the 1σ error, and S/N. Since the metallicity studies use only line ratios, we did not attempt to flux calibrate the spectrum, which is nontrivial in near-IR observations. The instrument response is essentially constant for the wavelength range from [O III] $\lambda 4363$ to [O III] $\lambda 5007$. The $\text{H}\alpha$ line lies in the region where the response has dropped by $\sim 35\%$. The response on the expected [N II] line position has dropped by $\sim 65\%$, which may be the reason that there is no

Table 1
Observed Line Intensities and Ratios

Ion Line (1)	z_{obs} (2)	Flux (3)	Flux (corrected) (4)	1σ (5)	S/N (6)
[N II] $\lambda 6584$...	<0.009	<0.025
$\text{H}\alpha$ $\lambda 6563$	1.705	3.12	5.03	± 0.4	13
[O III] $\lambda 5007$	1.706	6.45	6.45	± 0.3	15
[O III] $\lambda 4959$	1.705	1.98	1.98	± 0.3	10
$\text{H}\beta$ $\lambda 4861$	1.705	1.0	1.0	± 0.1	5
[O III] $\lambda 4363$	1.696	0.27	0.27	± 0.1	3
[O II] $\lambda 3727$	1.708	0.95	1.11	± 0.3	8

Notes. (1) Detected emission lines and their rest-frame wavelength. (2) Redshift calculated from the observed wavelength. (3) Measured flux, relative to $\text{H}\beta$, detector response uncorrected. (4) Measured flux, relative to $\text{H}\beta$, detector response corrected. (5) 1σ error of the line flux from Gaussian fitting. (6) Signal-to-noise of the line flux.

detection of [N II] within 3σ . After correcting for instrumental response, we obtain an upper limit for [N II]/ $\text{H}\alpha$. Metallicities were calculated using the following two methods.

1. *Strong line diagnostics.* In the absence of direct measurements from electron temperature, the ratio of strong nebular lines is used to determine the oxygen abundance. The well-known discrepancies between the different line ratio indicators can be removed by converting to the same base calibration following the methods of Kewley & Ellison (2008). We use the indicator $R_{23} = ([\text{O II}] \lambda 3727 + [\text{O III}] \lambda \lambda 4959, 5007)/\text{H}\beta$ to calculate metallicity. In our case, the upper and lower branch degeneracy of R_{23} can be broken by the upper limit of [N II]/ $\text{H}\alpha < 0.005$. In addition, the detection of the weak [O III] $\lambda 4363$ line almost certainly means the adoption of the lower branch. For the actual calculation, we use the lower branch calibration of McGaugh (1991) (M91 method) in the analytical form given by Kobulnicky et al. (1999). The resulting metallicity is $12 + \log(\text{O}/\text{H}) = 8.0$ in the M91 method. Converted to the Kewley & Dopita (2002) method (KD02), we have $12 + \log(\text{O}/\text{H}) = 8.1$ assuming zero extinction, or 8.3 assuming a high extinction value of $E(B - V) = 0.4$ (Cardelli et al. 1989; Osterbrock 1989). The high extinction value agrees with the direct estimate from the $\text{H}\alpha/\text{H}\beta$ in Table 1. However, because the $\text{H}\alpha$ line lies near the edge where the response has dropped by $\sim 35\%$, the ratio of $\text{H}\alpha/\text{H}\beta$ can be largely uncertain because it depends sensitively on the precision of correction for the detector response. Therefore, instead of using only the high extinction from $\text{H}\alpha/\text{H}\beta$, we use two extreme values of extinction to quantify the range of uncertainty caused by extinction. Note that the logarithm in the definition of $12 + \log(\text{O}/\text{H})$ means that 10% of change in the line ratio causes only ~ 0.04 dex change in metallicity. The uncertainty for our derived metallicity is therefore < 0.1 dex prior to extinction correction.
2. *Direct metallicity from electron temperature T_e .* The auroral line [O III] $\lambda 4363$ is often very weak, even in low metallicity environments. It is usually not observed in high metallicity galaxies without very sensitive, high S/N spectra (e.g., Garnett et al. 2004). The 3σ detection of [O III] $\lambda 4363$ in Lens22.3 strongly suggests a low metallicity environment. The ratio of [O III] $\lambda 5007$, 4959 and [O III] $\lambda 4363$ allows a direct measurement of the oxygen abundance via electron temperature T_e . We use the nebular package in IRAF to derive the electron temperature $T_e = 2.3557 \times 10^4$ K, assuming an electron density n_e of 100 cm^{-3} (T_e is relatively

insensitive to n_e , e.g., for $n_e = 1000 \text{ cm}^{-3}$, $T_e = 2.3508 \times 10^4 \text{ K}$). Following the procedure of Izotov et al. (2006), we obtain $12 + \log(\text{O}/\text{H}) = 7.5 \pm 0.1$ assuming zero extinction; or $12 + \log(\text{O}/\text{H}) = 7.3 \pm 0.1$ assuming a high extinction value of $E(B - V) = 0.4$.

The 0.6 dex discrepancy between the KD02 and T_e method is not surprising since the metallicity measured from the direct T_e method is systematically lower than other methods; such offsets can be as large as 0.7 dex (Liang et al. 2006; Yin et al. 2007; Nagao et al. 2006). Regardless of the offset between the two methods, both metallicity estimates indicate that Lens22.3 is low in oxygen abundance. The evidence that Lens22.3 is a star-forming galaxy instead of a narrow-line AGN comes from its position on the traditional Baldwin–Phillips–Terlevich (BPT) diagram (Baldwin et al. 1981). Using the upper limit of $[\text{N II}]/\text{H}\alpha$ and the ratio of $[\text{O III}]/\text{H}\beta$, Lens22.3 is located on the leftmost region of the star-forming branch of the BPT $[\text{N II}]$ diagram, excluding its possibility of being an AGN (Kewley et al. 2006).

3.2. Photometry

We searched the *Hubble Space Telescope* (HST) archive and obtained the photometry for Lens22.3. The observed AB magnitudes are 23.2 ± 0.1 , 23.6 ± 0.2 , 23.3 ± 0.1 , 23.4 ± 0.1 , and 23.1 ± 0.1 in the ACS g_{F475W} , r_{F625W} , i_{F775W} , z_{F850LP} , and NICMOS J_{F110W} bands, respectively. After correcting for the lensing magnification of 15.5 ± 0.3 (provided by J. Richard 2009, private communication), the absolute B -band magnitude is $M_B = -18.3 \pm 0.1$ (Vega System). A simple spectral energy distribution (SED) fitting using the *kcorrect* v4.1.4 code of Blanton & Roweis (2007) yields a stellar mass of $1.6 \times 10^9 M_\odot$. Since the *kcorrect* may overestimate the stellar masses of high-redshift galaxies (Blanton & Roweis 2007), we recalculated the stellar mass using the advanced version of the code LE PHARE (photometric redshift and simulation package; Ilbert et al. 2009) based on population synthesis models of Bruzual & Charlot (2003). The resulting stellar mass is $4.4 \pm 1.2 \times 10^8 M_\odot$.

3.3. Morphology and Kinematics

Thanks to the excellent seeing ($\sim 0''.4$) and the powerful magnification of gravitational lensing, the target is spatially resolved. In Figure 2, we show the HST F775W image in the vicinity of Lens22.3. The image has been registered onto the MOIRCS chip, which has a pixel scale of $0''.117 \text{ pixel}^{-1}$. The MOIRCS slit layout is shown, where X is the dispersion direction and Y is the spatial direction which is also along the elongated side of the galaxy. On the lower right corner is a zoomed image of Lens22.3, with various intensity contours overlaid. It has a clear double-nuclei-like morphology. The nuclei are separated by $\sim 0''.4$, corresponding to a physical scale of $\sim 3 \text{ kpc}$ at the redshift of $z = 1.7$. The intrinsic separation will be smaller than this value because the image has been elongated by lensing effects. We divide the two-dimensional spectrum into subsections A, B, C, D along the spatial direction Y , using a 3 pixel bin that roughly matches the average seeing of the observation. We extract the spectrum for apertures A, B, C, D using the strongest line $[\text{O III}] \lambda 5007$ and $\text{H}\alpha$. The velocity profile relative to the center of the subsections are given in Figure 3. For comparison, the velocity profile for the sky OH line nearest to $\text{H}\alpha$ extracted from the same apertures is also shown. There seems to be a systematic rise in the velocity from

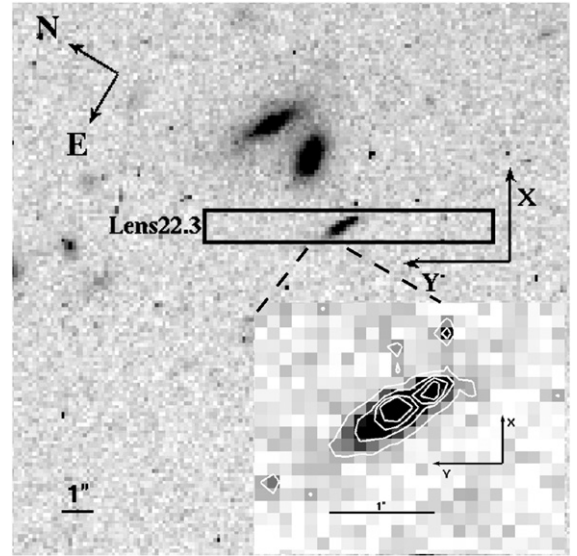


Figure 2. HST rescaled F775W image for the field of Lens22.3. The image has been rescaled and registered onto the MOIRCS chip. The slit on Lens22.3 has a width of $1''$ and a length of $9''$. Slit X (dispersion) and Y (spatial) directions are marked. A zoomed view of Lens22.3 with intensity contours (0.3, 0.2, 0.1, 0.04 of the peak intensity) is shown on the lower left corner.

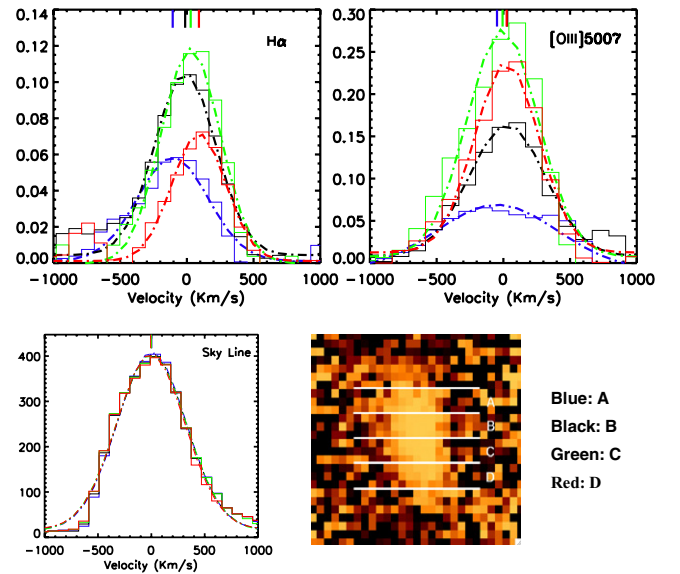


Figure 3. Top two panels: velocity profile of $\text{H}\alpha$ and $[\text{O III}]$ from spectra extracted within the spatial apertures A, B, C, D (bottom right panel). Bottom left panel: velocity profile for the sky line nearest to $\text{H}\alpha$ using the same apertures. Bottom right panel: two-dimensional spectrum of $\text{H}\alpha$, spatially cut into subapertures A, B, C, D. The velocity zero point is chosen to be the averaged center of the cuts.

A to D in $\text{H}\alpha$, but not in $[\text{O III}] \lambda 5007$. The misalignment of the line profile in the spatial direction and the double-nuclei-like morphology may indicate that the system is rotating or merging. Future follow-up with integral field spectroscopy with adaptive optics is highly desirable to reveal the kinematics of the system.

3.4. Mass–Metallicity Relation

In Figure 4, we show the mass/luminosity–metallicity relation for the local (Tremonti et al. 2004) and high-redshift (Erb et al. 2006) star-forming galaxies. All metallicities in Figure 4 have been rescaled to the same KD02 method using the calibration of Kewley & Ellison (2008). The local sample of Tremonti

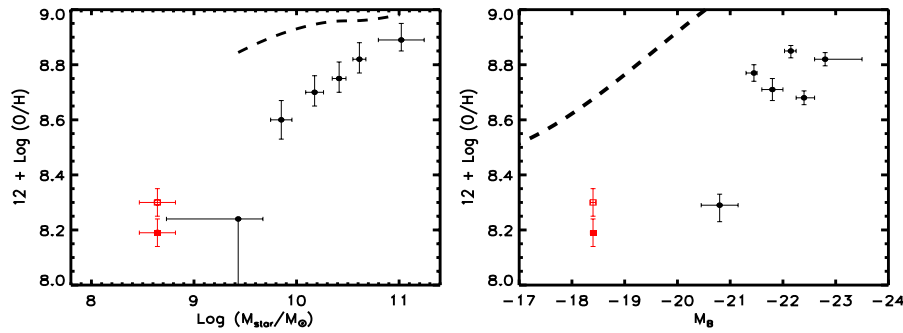


Figure 4. Left: mass–metallicity relation. Dashed line: local relation from the SDSS sample (Tremonti et al. 2004). Filled black circle: relation for galaxies $z \geq 2$ (Erb et al. 2006). Filled red square: Lens22.3, without extinction correction. Empty red square: Lens22.3, after extinction correction. Right: luminosity–metallicity relation. Dashed line: local relation from SDSS sample (Tremonti et al. 2004). Filled black circle: relation for galaxies $z \geq 2$ (Erb et al. 2006). Filled red square: Lens22.3, without extinction correction. Empty red square: Lens22.3, after extinction correction. All metallicities have been recalculated to the same base of KD02 (Kewley & Ellison 2008).

et al. (2004) is based on $\sim 53,000$ Sloan Digital Sky Survey (SDSS) star-forming galaxies and the Erb et al. (2006) sample is based on composite spectra of 87 rest-frame UV-selected star-forming galaxies at $z \geq 2$. Lens22.3 is consistent with the mass/luminosity–metallicity relation of the high- z sample. We evaluate the effect of extinction assuming a high extinction value of $E(B - V) = 0.4$. Extinction causes metallicity to rise by ~ 0.1 dex, but it does not significantly change the position of Lens22.3 on the mass–metallicity diagram. Lens22.3 is currently the lowest mass system with direct measurement on the mass–metallicity relation diagram; Lens22.3 extends the luminosity–metallicity relation to the fainter end by more than an order of magnitude, demonstrating the capability of using gravitationally lensed samples to probe intrinsically fainter and less massive systems than are found in existing samples.

4. SUMMARY

We reported the discovery of a low-metallicity star-forming galaxy at $z = 1.7$. We detect the temperature sensitive auroral line [O III] $\lambda 4363$ which allows us to derive metallicity using the direct T_e method for the first time at high redshift. The low metallicity and low luminosity/mass of the $z = 1.7$ star-forming galaxy place it at the lowest end of the mass/luminosity–metallicity relation, extending the $z > 2$ luminosity–metallicity relation by more than an order of magnitude. Our ongoing near-IR spectroscopic survey of lensing clusters aims to obtain metallicities for more objects like Lens22.3 in the redshift range $1.5 < z < 3$.

We want to thank the referee for her/his valuable comments and suggestions that significantly improved this Letter. We thank Johan Richard for providing us with the lensing magnification of Lens22.3, and Youichi Ohyama for his help with MOIRCS data reduction. We also thank Katelyn Allers for useful discussion on Telluric correction methods and C.-J. Ma for running the LE PHARE code for us. We recognize and acknowledge the very significant cultural role and reverence that the summit of Mauna Kea has always had within the indigenous Hawaiian community. We appreciate the opportunity to conduct observations from this sacred mountain.

Facilities: Subaru (MOIRCS)

REFERENCES

- Baldwin, J. A., Phillips, M. M., & Terlevich, R. 1981, *PASP*, **93**, 5
 Blanton, M. R., & Roweis, S. 2007, *AJ*, **133**, 734
 Broadhurst, T., et al. 2005, *ApJ*, **621**, 53
 Bruzual, G., & Charlot, S. 2003, *MNRAS*, **344**, 1000
 Cardelli, J. A., Clayton, G. C., & Mathis, J. S. 1989, *ApJ*, **345**, 245
 Daddi, E., Cimatti, A., Renzini, A., Fontana, A., Mignoli, M., Pozzetti, L., Tozzi, P., & Zamorani, G. 2004, *ApJ*, **617**, 746
 Erb, D. K., Shapley, A. E., Pettini, M., Steidel, C. C., Reddy, N. A., & Adelberger, K. L. 2006, *ApJ*, **644**, 813
 Erb, D. K., Shapley, A. E., Steidel, C. C., Pettini, M., Adelberger, K. L., Hunt, M. P., Moorwood, A. F. M., & Cuby, J.-G. 2003, *ApJ*, **591**, 101
 Frye, B. L., et al. 2007, *ApJ*, **665**, 921
 Garnett, D. R., Edmunds, M. G., Henry, R. B. C., Pagel, B. E. J., & Skillman, E. D. 2004, *AJ*, **128**, 2772
 Hayashi, M., et al. 2009, *ApJ*, **691**, 140
 Hoyos, C., Koo, D. C., Phillips, A. C., Willmer, C. N. A., & Guhathakurta, P. 2005, *ApJ*, **635**, L21
 Ichikawa, T., et al. 2006, *Proc. SPIE*, **6269**, 38
 Ilbert, O., et al. 2009, arXiv:0903.0102
 Izotov, Y. I., Stasińska, G., Meynet, G., Guseva, N. G., & Thuan, T. X. 2006, *A&A*, **448**, 955
 Kakazu, Y., Cowie, L. L., & Hu, E. M. 2007, *ApJ*, **668**, 853
 Kewley, L. J., & Dopita, M. A. 2002, *ApJS*, **142**, 35
 Kewley, L. J., & Ellison, S. L. 2008, *ApJ*, **681**, 1183
 Kewley, L. J., Groves, B., Kauffmann, G., & Heckman, T. 2006, *MNRAS*, **372**, 961
 Kobulnicky, H. A., Kennicutt, R. C., & Jr Pizagno, J. L. 1999, *ApJ*, **514**, 544
 Lemoine-Busserolle, M., Contini, T., Pelló, R., Le Borgne, J.-F., Kneib, J.-P., & Lidman, C. 2003, *A&A*, **397**, 839
 Liang, Y. C., Yin, S. Y., Hammer, F., Deng, L. C., Flores, H., & Zhang, B. 2006, *ApJ*, **652**, 257
 Limousin, M., et al. 2007, *ApJ*, **668**, 643
 McGaugh, S. S. 1991, *ApJ*, **380**, 140
 Nagao, T., Maiolino, R., & Marconi, A. 2006, *A&A*, **459**, 85
 Nesvadba, N. P. H., et al. 2007, *ApJ*, **657**, 725
 Osterbrock, D. E. 1989, *Astrophysics of Gaseous Nebulae and Active Galactic Nuclei* (Mill Valley, CA: Univ. Science Books), **422**
 Pettini, M., Rix, S. A., Steidel, C. C., Adelberger, K. L., Hunt, M. P., & Shapley, A. E. 2002, *ApJ*, **569**, 742
 Pettini, M., Steidel, C. C., Adelberger, K. L., Dickinson, M., & Gialavisco, M. 2000, *ApJ*, **528**, 96
 Richard, J., Stark, D. P., Ellis, R. S., George, M. R., Egami, E., Kneib, J.-P., & Smith, G. P. 2008, *ApJ*, **685**, 705
 Shapley, A. E., Erb, D. K., Pettini, M., Steidel, C. C., & Adelberger, K. L. 2004, *ApJ*, **612**, 108
 Stark, D. P., Swinbank, A. M., Ellis, R. S., Dye, S., Smail, I. R., & Richard, J. 2008, *Nature*, **455**, 775
 Steidel, C. C., Adelberger, K. L., Shapley, A. E., Pettini, M., Dickinson, M., & Gialavisco, M. 2003, *ApJ*, **592**, 728
 Steidel, C. C., Gialavisco, M., Pettini, M., Dickinson, M., & Adelberger, K. L. 1996, *ApJ*, **462**, L17
 Tokoku, C., et al. 2006, *Proc. SPIE Conf. Ser.*, **6269**, 62694N
 Tremonti, C. A., et al. 2004, *ApJ*, **613**, 898
 Yee, H. K. C., Ellingson, E., Bechtold, J., Carlberg, R. G., & Cuillandre, J.-C. 1996, *AJ*, **111**, 1783
 Yin, S. Y., Liang, Y. C., Hammer, F., Brinchmann, J., Zhang, B., Deng, L. C., & Flores, H. 2007, *A&A*, **462**, 535